Influence of Nickel-Coated Nanostructured WC-Co Powders on Microstructural and Tribological Properties of HVOF Coatings

M. Jafari, M.H. Enayati, M. Salehi, S.M. Nahvi, S.N. Hosseini, and C.G. Park

In this research, a novel nickel-coated nanostructured WC-12Co powder (Ni/nc-WC) was developed and used as feedstock material for high velocity oxygen fuel process. The Ni/nc-WC powders with average WC grain size of ~15 nm were produced by mechanical milling and electroless plating processes. The microstructural and tribological characteristics of Ni/nc-WC coating were investigated and compared with those of microcrystalline WC-12Co (mc-WC) and nanostructured WC-12Co (nc-WC) coatings. X-ray diffractometry, high-resolution field emission scanning electron microscopy, and transmission electron microscopy were used to evaluate the microstructure of the powders and coatings. A ball-on-disk technique was used to probe the wear behavior of the coatings. The Ni/nc-WC coating showed negligible decarburization of ~5.4%, while mc-WC and nc-WC coatings suffered from higher decarburization levels of 16.3 and 36.8%. The wear rate of Ni/nc-WC coating was 2.5×10^{-4} mg/m indicating ~75 and 82% increase in wear resistance compared with mc-WC and nc-WC coatings. The wear track analysis of mc-WC and nc-WC coatings showed evidences of delamination mechanism. Besides, a severe carbide pullout mechanism was operative in wear of nc-WC coating. As for Ni/nc-WC coating, individual carbide pullout following the elimination of Ni(Co) matrix was the predominant wear mechanism.

1. Introduction

Sintered nanostructured WC-Co materials are widely used in a variety of industrial applications such as cutting and drilling tools, extrusion dies, etc., due to their superior combination of hardness and fracture toughness (Ref 1-4). As the WC grain size decreases to the nanometer scale, the mean free path of cobalt matrix is reduced leading to a greater constraint against deformation and binder phase extrusion. Therefore, higher hardness and wear resistance are obtained for the sintered nanostructured WC-Co as compared to their conventional counterparts (Ref 5-8).

The same approach of using nanostructured WC-Co powders has been the subject of many investigations (Ref 5, 8-13) to improve the wear resistance of WC-Co

coatings mostly deposited by the high velocity oxygen fuel (HVOF) technique. However, many studies have reported inferior wear performance for HVOF-sprayed nanostructured WC-Co coatings compared to the conventional microcrystalline ones (Ref 9, 14-16). This behavior is attributed to the higher surface-to-volume ratio of nanostructured WC particles, which makes them more susceptible to decomposition and decarburization during HVOF process, causing the formation of brittle phases such as W_2C, metallic tungsten, and amorphous or nanostructured Co-W-C compounds in the coating microstructure. The effect of these non-WC phases has been reported to be deleterious to the wear performance of WC-Co coatings (Ref 8, 9, 12, 13, 17, 18). Therefore, numerous investigations have been directed toward decreasing the extent of WC decarburization during HVOF spraying of nanostructured WC-Co powders so as to achieve superior wear resistance for the coatings, e.g., reducing the flame temperature using high velocity air fuel (HVAF) process (Ref 19), using reductive combustion flame (Ref 10), optimization of HVOF parameters such as fuel/oxygen ratio (Ref 16, 20, 21) and in-flight particle velocity (Ref 22), etc. Besides the optimization of HVOF process, modification of the nanostructured WC-Co feedstock powders has been of great interest to reduce WC decarburization during spraying. These attempts include using bimodal (Ref 9, 19) and multimodal (Ref 11) feedstock powders consisting of both nano- and microcrystalline WC-Co powders, and heat treatment of

M. Jafari, M.H. Enayati, M. Salehi, and **S.N. Hosseini**, Department of Materials Engineering, Isfahan University of Technology, 84156-83111 Isfahan, Iran; **S.M. Nahvi**, Steel Institute, Isfahan University of Technology, 84156-83111 Isfahan, Iran; and **C.G. Park**, Department of Materials Science and Engineering, Pohang University of Science and Technology (POSTECH), Pohang 790-784, Republic of Korea. Contact e-mail: majid_jafari@ma.iut.ac.ir.

spray-dried ultrafine WC-Co powders (Ref 18). In addition, the idea of using metal-clad WC-Co feedstock powders (Ref 6, 7, 13) has been recently reported to limit the extent of decarburization during HVOF process. In this respect, Baik et al. Ref 13 prepared Co-coated WC-Co nanocomposite powders by immersing them into Co-hydrate sol and subsequent hydrogen reduction. Their results showed improvement in abrasion wear resistance of the resultant coating as a consequence of lower WC decarburization, although the W_2C phase was still one of the main constituents of phase composition of the coating. Mateen et al. (Ref 6) and Saha et al. (Ref 7) used near-nanostructured WC-Co powders with a duplex cobalt layer developed by chemical vapor deposition (CVD) process. They found that the presence of Co layer around WC-Co prevents significant WC decarburization during HVOF spraying leading to a higher wear and corrosion resistance compared to the conventional coatings.

In the present study, a novel electroless nickel-coated nanostructured WC-12Co powder was developed and used as HVOF feedstock materials. The characteristics of resultant nanostructured coating were investigated in terms of microstructural, mechanical, and sliding friction and wear properties.

2. Experimental

2.1 Materials and Methods

In this study, a commercial microcrystalline WC-12Co powder (denoted as mc-WC) from Metallization Ltd. was used as starting material. This powder is manufactured by agglomeration and sintering process and contains micron-sized WC with size of 1-6 μm. In order to obtain nanostructured WC-12Co powder (referred as nc-WC), the initial mc-WC powder was milled in a planetary ball mill (Retsch PM 100) under argon atmosphere. The milling media consisted of a 500 mL volume vial and 20 grinding balls (hardened steel) with a diameter of 20 mm. Ball milling was performed with ball-to-powder ratio of 10:1, packing ratio of 40% and rotation speed of 250 rpm for 20 h. To produce nickel-coated nanostructured WC-12Co powder (referred as Ni/nc-WC), the as-milled powder is subjected to an electroless nickel plating process [bath #18071, Electroless Nickel SLOTONIP 70A process from Schloetter Galvanotechnik (Ref 23)] with parameters specified in Table 1.

Table 1 Parameters of electroless nickel plating

Parameter	Value
Bath composition (mL/L)	
Slotonip 71-1 (basic solution)	160
Slotonip 72 (Nickel solution)	70
Slotonip 76 (Stabilizer)	7
HF (40 vol.%)	12
Ammonia Solution (25 vol.%)	To adjust pH
Temperature (°C)	80-82
Time (h)	2
pH	4.5-5

The spray drying process was carried out on the as-synthesized nc-WC and Ni/nc-WC powders to obtain agglomerated particles with appropriate flow-ability and narrow size distribution required for HVOF thermal spray process. Prior to spray drying, the powders were mixed with 0.75 wt.% polyvinyl alcohol (PVA) and 40 wt.% distilled water to form stable slurry. The spray-dried particles were collected and sieved to achieve particle size in the range of 20-45 μm using a vibratory sieve shaker (Fritsch, Analysette 3 Pro type). Particle size of the powders was assessed using a particle size analyzer (Mastersizer 2000). Moreover, the flow-ability test was carried out by measuring the time required for natural flow of 50 g powders passing through a standard funnel.

Chemical composition of mc-WC, nc-WC, and Ni/nc-WC powders was identified using atomic absorption spectroscopy (Young Lin AAS-8010).

ST37 steel disks with the size of Ø30 × 5 mm were used as substrate. Prior to spraying, the disks were grit blasted to obtain mean surface roughness (Ra) ~15 ± 2 μm and were degreased with acetone.

The feedstock powders were deposited on the steel substrates by HVOF spraying using MET JET III HVOF torch (Metallisation Ltd. at PACO, Isfahan, Iran) with parameters listed in Table 2. The resultant coatings are denoted as ''mc-WC,'' ''nc-WC,'' and ''Ni/nc-WC'' coatings.

2.2 Microstructural Characterization

In order to identify the phase composition, the XRD patterns of the powders and coatings were recorded with step size of 0.05° per 1 s using a Philips diffractometer (40 kV) with Cu Kα radiation ($k = 0.15406$ nm). The patterns were then characterized by PANalytical X'Pert High Score software. High Resolution FE SEM (JEOL JSM-7401F) was used to evaluate the morphological and microstructural characteristics of powders and coatings. Carbon content of the initial powders and the coatings was measured by an elemental analysis tool (Elementar Vario EL III, Germany) to quantify the amount of carbon loss during the HVOF process.

The XRD peak broadening, high-resolution FE SEM, and high-resolution TEM (JEOL JEM-2100F) were applied to determine the WC grain size in the nanostructured powders and coatings. The TEM sampling from the coatings was performed via lift-out method using focused ion beam (FIB) technique (FEI Company, USA).

Table 2 HVOF spray parameters

Deposition parameter	Value
Spraying distance (mm)	350
Oxygen (mL/min)	830
Methane (mL/min)	260
Carrier gas (Nitrogen) (L/min)	4
Oxygen/fuel ratio	3.19
Powder feed rate (g/min)	40
Spray angle (°)	90

In the case of XRD peak broadening approach, to quantify the accurate WC grain size by considering the effect of internal lattice strain, the Stokes and Wilson's formula was used (Ref 24):

$$\beta = \beta_{\mathrm{d}} + \beta_{\varepsilon} = \frac{0.89\lambda}{d\,\cos\theta} + (4\varepsilon)\tan\theta, \tag{Eq 1}$$

where β is the full width at half maximum (FWHM) of the diffraction peak after instrument correction; β_{d} and β_{ε} are FWHM due to the small grain size and internal lattice strain, respectively; θ is the Bragg diffraction angle, λ is the wavelength of x-ray used, d is the average grain size, and ε is the average internal lattice strain. The correction of instrumental line broadening was done utilizing pure WC powders with the size of ~5-10 μm as a reference. Hence, the diffraction line broadening (β) was measured as follows (Ref 25):

$$\beta^2 = \beta_{\exp}^2 - \beta_{\mathrm{ins}}^2, \tag{Eq 2}$$

where $\beta_{\exp}$ and β_{ins} are FWHM of the peaks related to the experimental and instrumental broadening profiles, respectively. The average grain size can be estimated from intercept of (β·cos θ) versus (sin θ) line at sin θ = 0.

To determine the porosity of coatings, the SEM images from coatings cross section were digitized and analyzed using Clemex microscopy image analysis software. The thickness of deposited coating layer was measured by Elcometer coating thickness gage. The surface roughness (Ra) values of the as-sprayed coatings were measured by Taylor-Hobson roughness tester.

2.3 Mechanical Properties

The micro-hardness test (Buehler micro-indentation) was performed by taking ten indents along the mid-plane of coatings cross section under 2 kg of applied load.

The fracture toughness (K_{IC}) of the coatings was measured using indentation technique under 5 kg of applied load. The quantitative analysis of fracture toughness was executed using Eq 3, assuming that the cracks generated from indentations are radial with the Palmqvist geometry (Ref 26):

$$K_{\mathrm{IC}} = 0.0193(H_{\mathrm{v}}d)\left(\frac{E}{H_{\mathrm{v}}}\right)^{\frac{2}{5}}(a)^{-\frac{1}{2}}, \tag{Eq 3}$$

where H_{v} and E are Vickers hardness and elastic modulus of the coatings, a is the crack length from indenter corner, and d is the half-diagonal of the Vickers indentation.

The elastic modulus of the coatings was calculated from the initial slope of force-displacement diagram during unloading step of nano-indentation test (Hysitron, PI-85, USA) as proposed by Oliver and Pharr (Ref 27).

2.4 Friction and Wear Properties

The sliding friction and wear behavior of the coatings were investigated using a ball-on-disk wear test machine under un-lubricated conditions. The parameters of sliding test are presented in Table 3.

Table 3 The parameters of sliding wear test

Parameter	Value
Sliding distance (m)	3000
Vertical load (N)	30
Sliding speed (m/s)	0.1
Temperature (°C)	25
Humidity (%)	28-30

Prior to wear testing, the coatings were ground and polished down to 1 μm resulting in the mean surface roughness values in the range of 0.05-0.1 μm. Sintered alumina balls (from TIS Wälzkörpertechnologie GmbH, Germany) with a diameter of 7 mm, apparent density of 3.95 g/cm³, and hardness of 70 HRC were used as counterface. The wear loss was measured from the mass difference of specimens before and after sliding test using an electronic weighing balance with an accuracy of 0.01 mg. The friction coefficient was continuously recorded with sliding distance. In order to take the repeatability into account, the results for the sliding tests were acquired from the average of three readings. To investigate the wear mechanism of the coatings, the morphology and elemental analysis of worn surfaces were examined by high-resolution FE SEM equipped with energy dispersive spectroscopy (EDS).

3. Results and Discussion

3.1 Characterization of Feedstock Powders

Figure 1 shows the morphology of mc-WC and nc-WC powders. The mc-WC powder particles (Fig. 1a) have a spherical morphology with a particle size in the range of 15-45 μm. As observed in Fig. 1(b-e), intensive WC-Co particle size reduction to ~100-500 nm has occurred due to the high impact forces applied on the powders during milling. Higher magnification images (Fig. 1d, e) reveal a flake-like morphology for the as-milled nc-WC particles in which the nanostructured WC particles are distributed. In the early stages of ball milling, the soft Co matrix is plastically deformed and becomes flattened as a result of high impact energy of the balls. Concurrently, the WC particles are broken and embedded into the Co matrix (Ref 28). With an increase in the milling time, due to the substantial strain hardening, the WC-Co particles are exposed to successive fragmentation leading to the uniform distribution of refined WC particles within Co matrix.

Figure 1(f) illustrates the morphology of nc-WC powders after spray drying. The resulting powders are found to have adequate particle size in a range of 5-50 μm with a majority of ~38 μm and suitable morphology, both of which are required for high quality HVOF spraying. The flow-ability test results showed the average flow-ability time of 15.5 s/50 g for spray-dried nc-WC particles indicating a slightly higher value than that of mc-WC powders (12.6 s/50 g).

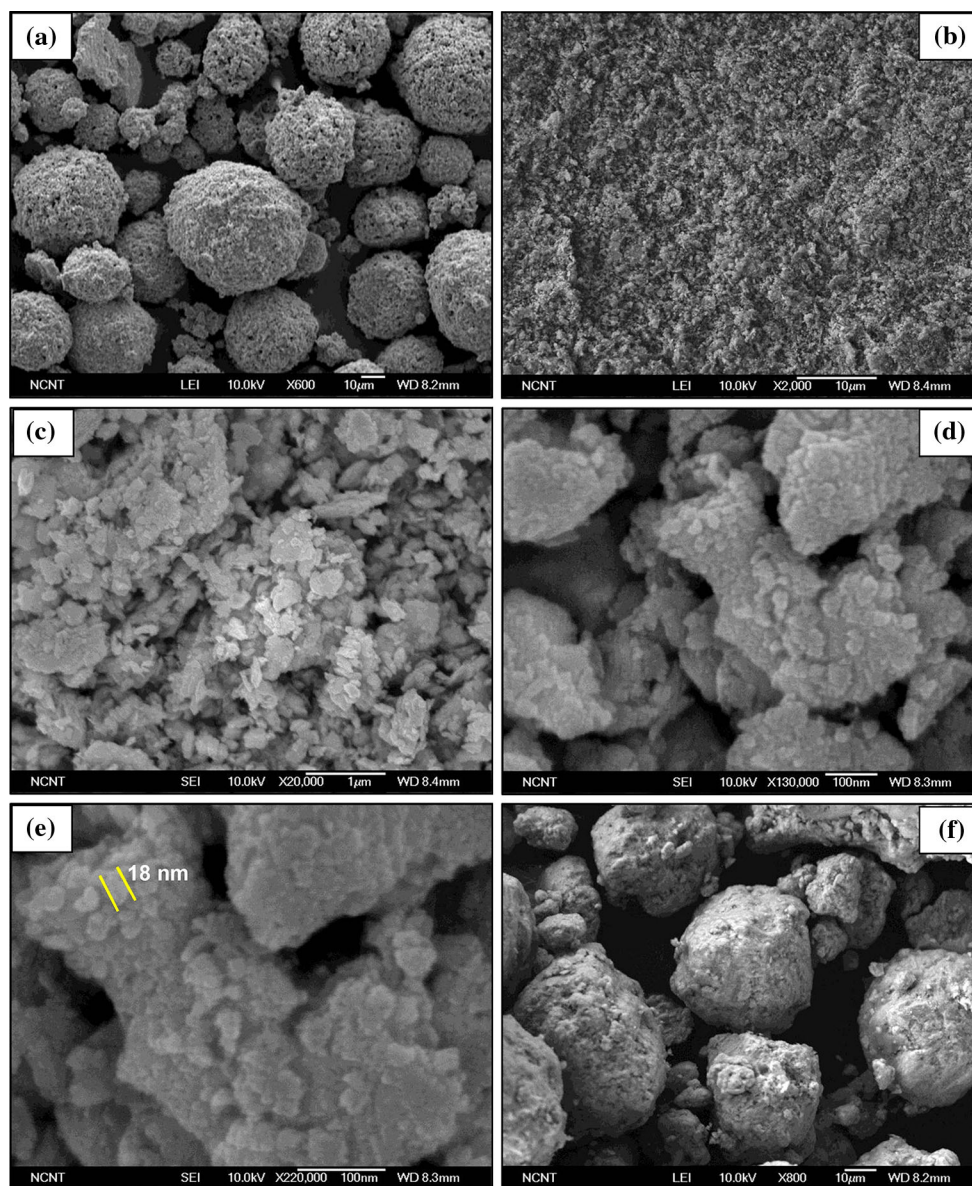Figure 2 demonstrates the XRD patterns of different feedstock powders.

Fig. 1 SEM images from (a) mc-WC, (b-e) as-milled nc-WC at different magnifications, and (f) spray-dried nc-WC powders

As shown in Fig. 2(a), mc-WC powder consists of WC and Co phases. The XRD pattern of nc-WC reveals WC peak broadening and Co peak disappearance. The broadening of WC peaks is attributed to the significant grain refinement during ball milling (Ref 28-30). The average grain size and internal lattice strain of WC phase, determined based on three WC peaks of $(100)_{WC}$, $(101)_{WC}$ and $(110)_{WC}$ using Eq 1, were found to be ~15 nm and 1.1%, respectively. The WC grain size estimated by XRD peak broadening approach is supported by SEM (Fig. 1e) and TEM observations of nc-WC (Fig. 3), which confirm that nanostructured WC with grain size of 5-30 nm is uniformly distributed within the Co matrix.

Figure 4(a, b) illustrates the surface morphology of as-synthesized Ni/nc-WC.

The appearance of cauliflower-like structure for Ni/nc-WC, which is the main characteristics of the microstructure of electroless coating (Ref 31-33), proves that the individual nc-WC powder particles are covered by nickel coating. The cross-section image of Ni/nc-WC powders (Fig. 4c) reveals that a very thin and uniform nickel layer with a thickness of <100 nm is formed around nc-WC particles. The spray-dried Ni/nc-WC powders (Fig. 4d) have the particle size range of 5-45 μm with the majority of ~32 μm, average flow-ability of 15.2 s/50 g and appropriate morphology for HVOF spraying. The XRD analysis of Ni/nc-WC powders (Fig. 2c) shows a similar pattern to nc-WC, signifying that the formation of a thin nickel layer has not changed the inner structure of nc-WC particles.

The characteristics of different feedstock powders in terms of chemical composition, particle size, and carbide size are summarized in Table 4.

3.2 Characterization of Coatings

3.2.1 Microstructure. The cross-sectional SEM images of mc-WC, nc-WC, and Ni/nc-WC coatings are illustrated in Fig. 5. The characteristics of the coatings including porosity percentage, thickness, and surface roughness are also compared in Table 5.

According to the data given in Table 5, the lowest porosity of ~0.5% is obtained for Ni/nc-WC coating, while mc-WC and nc-WC show higher values of ~1.6 and 0.8%, respectively. The lower porosity of Ni/nc-WC coating can be attributed to the presence of Ni outer layer around WC-Co particles, which provides more uniform plastic flow for in-flight particles on impact to the substrate thereby improving the inter-splat cohesion (Ref 6).

The surface roughness values reveal greater smoothness for two nanostructured coatings (i.e., nc-WC and Ni/nc-WC) with respect to mc-WC one. This is partly due to the extremely finer WC grains in the nanostructured WC-Co powders than mc-WC one (Ref 16).

The XRD patterns of mc-WC, nc-WC, and Ni/nc-WC are presented in Fig. 6(a).

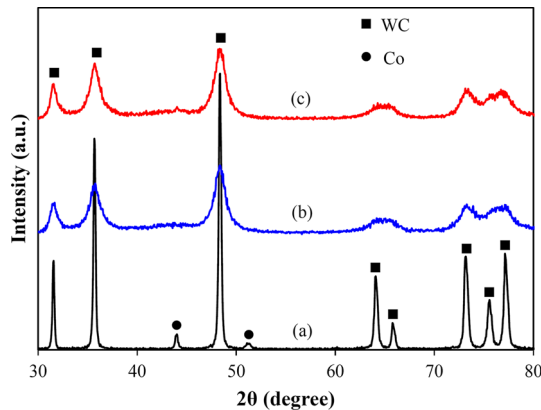The XRD pattern of mc-WC coating reveals the presence of W_2C and η (Co_6W_6C) phases. Moreover, XRD peaks of cobalt disappeared indicating that most of the cobalt binder phase has reacted with tungsten and carbon to form η phase. This phase composition verifies that decarburization of WC phase takes place during HVOF spraying of mc-WC coating. Based on carbon content analysis, the extent of decarburization for mc-WC coating was found to be ~16.3%. According to the literature (Ref 8, 9, 14, 15, 20), the high temperature of HVOF flame (~3000 °C) causes the melting of cobalt matrix (with melting point of ~1495 °C). Subsequently, the WC dissolution into the liquid matrix takes place enriching the surrounding cobalt in both tungsten and carbon. Due to the oxidizing atmosphere of HVOF flame, the carbon dissolved in the matrix is oxidized to form CO/CO_2. This is followed by W_2C precipitation from the tungsten-rich cobalt matrix during solidification upon impact on the substrate. Another mechanism for decarburization and W_2C formation, as proposed by Guilemany et al. Ref 9, 34, is direct WC oxidation due to the exposure to HVOF flame at the free surface of the powder leading to the carbon loss through a solid state reaction.

In the case of nc-WC coating, the W_2C peaks with higher intensity are observed on the XRD pattern. This result, together with higher WC decarburization level of ~36.8%, confirms that nc-WC powder particles undergo more severe decarburization during HVOF spraying as compared to mc-WC. It can be explained that nanostructured WC particles with a higher surface area-to-volume ratio suffer from significantly faster dissolution into liquid cobalt, leading to the greater level of decarburization (Ref 14, 21, 29).

In contrast, the Ni/nc-WC coating is mainly composed of WC and Ni (Co) phases. The XRD pattern of Ni/nc-WC also shows a very small W_2C peak with substantially lower intensity with respect to that of mc-WC and nc-WC coatings. According to the carbon content analysis results, the level of WC decarburization of Ni/nc-WC coating is ~5.4%, representing about 66 and 85% decrease in the extent of decarburization in comparison to mc-WC and nc-WC coatings, respectively. As a result, severe decarburization of nanostructured WC during HVOF spraying is noticeably prevented owing to the protection role of
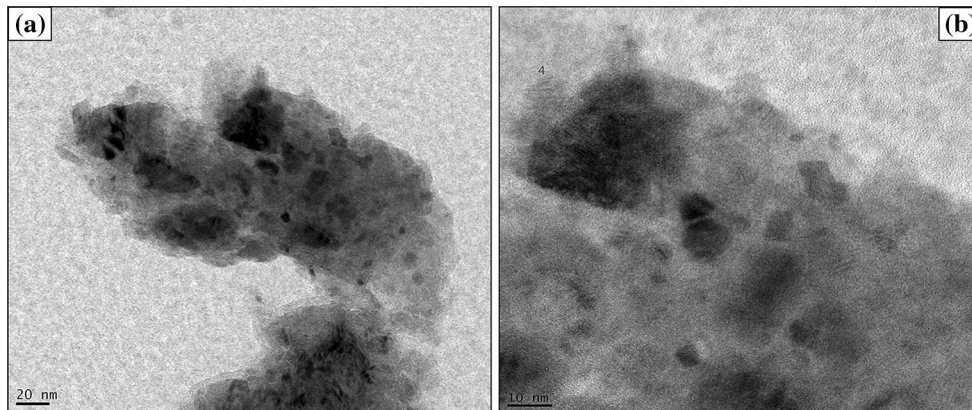

Fig. 2 The XRD patterns of (a) mc-WC, (b) nc-WC, and (c) Ni/nc-WC powders

Fig. 3 (a, b) The bright-field TEM images from nc-WC powders at different magnifications
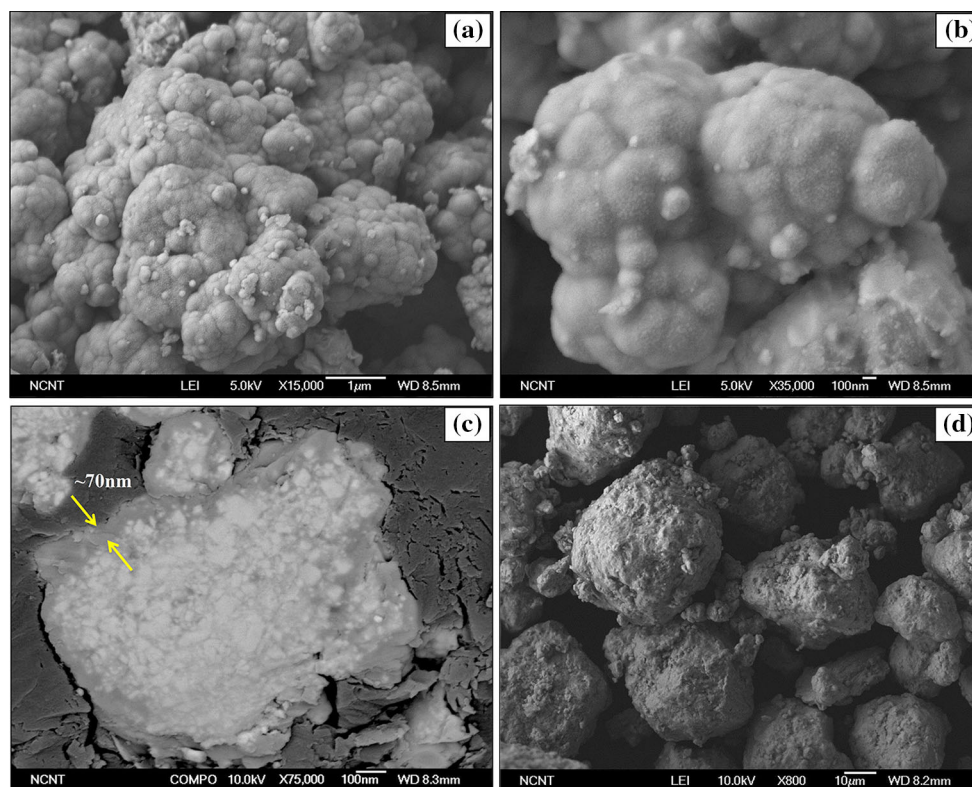
Fig. 4 SEM images from Ni/nc-WC particles: (a, b) surface morphology, (c) cross section, and (d) morphology after spray drying

Table 4   Comparison between the characteristics of feedstock powders

Powder	Preparation method	Chemical composition (wt.%) ($\pm$1%)					Particle size (μm)	Carbide size
		W	C	Co	Ni	Others		
mc-WC	As-received (agglomerated/sintered)	Balance	5.3	12.1	···	0.8	15-45	1-6 μm
nc-WC(a)	As-received (agglomerated/sintered)-mechanical milling-spray drying	Balance	5.3	11.8	···	1.1	5-50	5-30 nm
Ni/nc-WC(a)	As-received (agglomerated/sintered)-mechanical milling-electroless nickel plating-spray drying	Balance	5.3	11.4	3.4	1.3	5-45	5-30 nm

(a)The composition of nc-WC and Ni/nc-WC powders is identified after spray drying process

thin nickel layer around nc-WC powders. The mechanisms by which nickel layer around Ni/nc-WC particles decreases the extent of WC decarburization can be explained from two aspects. Firstly, the outer nickel layer melts during HVOF and absorbs latent heat of fusion. This causes a lower heating degree for inner nanostructured WC-Co particles, preventing an excessive WC dissolution into the matrix. The less the WC dissolution into the matrix, the less the subsequent dissolved carbon oxidation, leading to the lower extent of WC decarburization.

Secondly, the nickel layer around Ni/nc-WC particles can effectively reduce the WC exposure to oxidizing HVOF flame at the gas/powder interface, preventing direct WC oxidation and W_2C formation through a solid state reaction.

Figure 7 shows representative back-scattered electron (BSE) images from cross section of mc-WC coating.

As illustrated in Fig. 7, two different regions can be observed in the microstructure of mc-WC coating. The first region is identified by distribution of angular shape carbide particles in a dark matrix indicating negligible WC dissolution into the cobalt binder phase. The second region consists of a brighter matrix in which WC particles with more rounded morphology are distributed. Besides, some of the WC particles are either partially or completely enclosed by an irregular shape W_2C fringe with brighter contrast suggesting that WC particles probably act as nucleation sites for W_2C precipitation (Ref 9, 34). This feature corresponds to the part of in-flight particles which have locally experienced higher temperatures
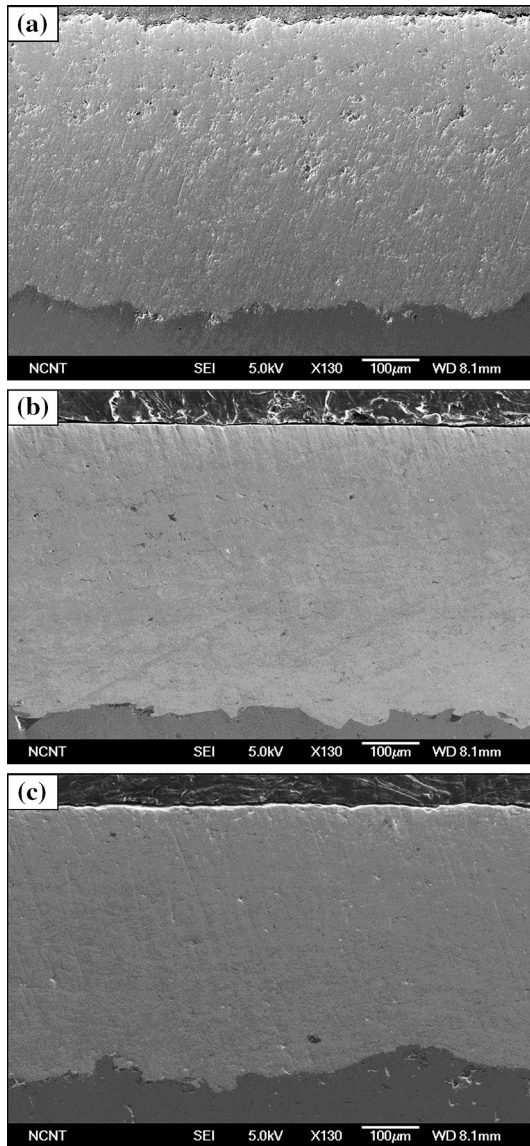
Fig. 5 The cross-sectional SEM images of (a) mc-WC, (b) nc-WC, and (c) Ni/nc-WC coatings

Table 5 Comparison between properties of the coatings

Coating	Porosity (%)	Thickness (μm)	Surface roughness (μm)
mc-WC	1.6 ± 0.5	417 ± 25	5.6 ± 0.6
nc-WC	0.8 ± 0.1	412 ± 20	2.8 ± 0.2
Ni/nc-WC	0.5 ± 0.1	394 ± 32	3.1 ± 0.3

during HVOF process leading to the partial WC dissolution into the Co matrix and subsequent WC decarburization (Ref 9, 27).

The cross-sectional BSE images from the microstructure of nc-WC coating (Fig. 8a, b) show different shades of gray contrast for Co matrix signifying different levels of WC dissolution into the binder phase. The angular carbide particles are located within the dark areas of matrix
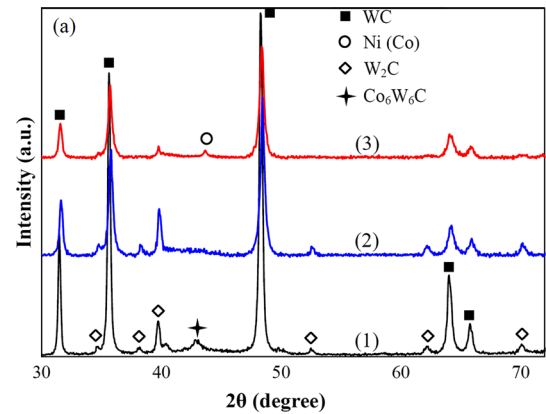

Fig. 6 XRD patterns of mc-WC (1), nc-WC (2), and Ni/nc-WC (3) coatings

resulting from the negligible WC dissolution. Besides, the large number of bright rounded particles along with core WC particles surrounded by W_2C rim is observed in the bright matrix pointing to the partial dissolution of WC into the Co matrix. A lamellar band-like structure is also present in the nc-WC coating microstructure. Formation of this structure, known as amorphous Co-W-C phase with higher degree of bright contrast, originates from the extensive dissolution of nanostructured WC into the liquid Co binder (Ref 5, 8, 14, 20, 35). The bright-field TEM image and selected area diffraction (SAD) analysis of nc-WC coating are shown in Fig. 8(c). The TEM observation of WC particle reveals a high density of structural defect, typically dislocations, in agreement with results obtained by Guilemany et al. Ref 34. It is believed that these defects were introduced to WC particles due to the severe deformation of high velocity in-flight particles on impact to the substrate. The TEM observations on other regions of nc-WC coating demonstrate the presence of discrete rounded particles in the matrix. The SAD pattern of the matrix shows diffuse rings of an amorphous phase indicating that substantial dissolution of WC particles into the Co binder has occurred to form amorphous Co-W-C phase (Ref 20). Moreover, the SAD pattern of a rounded particle confirmed this to be a W_2C particle as indexed in Fig. 8(c). This suggests that rounded W_2C particles with a smooth curvature interface with matrix may have independently precipitated from W-rich Co binder.

Contrary to the mc-WC and nc-WC, the Ni/nc-WC coating (Fig. 8d, e) is made up of ultrafine and nanostructured WC particles with a homogenous distribution within the dark Ni (Co) matrix. No significant evidences of decarburization such as core WC particles surrounded by W_2C fringe, isolated W_2C particles, and band-like structure can be observed in the coating microstructure. The TEM image and SAD analysis (Fig. 8f) also confirm the presence of nanostructured WC particles embedded in Ni (Co) matrix most of which have retained their angular morphology. It is suggested that due to the protection role of nickel layer around nanostructured WC-Co particles, which reduces the interaction between nanostructured
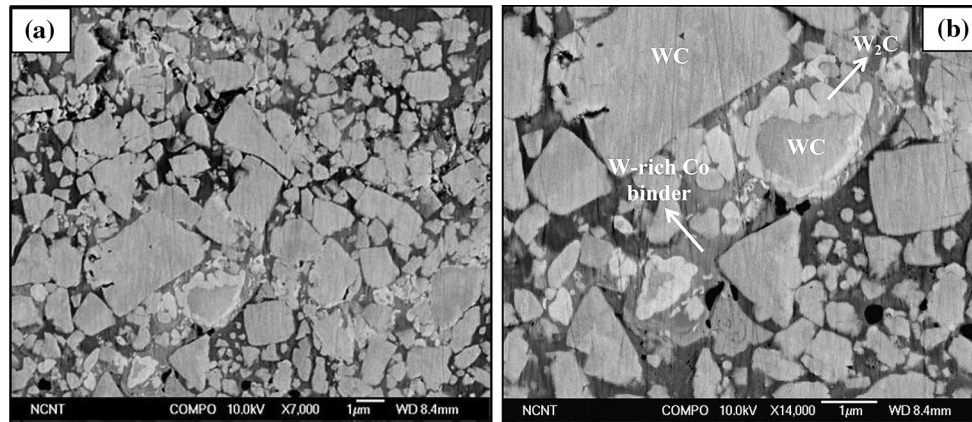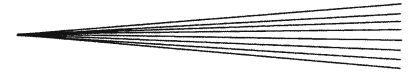
Fig. 7 BSE images from microstructure of mc-WC coating at different magnifications

WC and HVOF flame, the in-flight particles have passed through the spraying process without reaching temperature high enough for WC dissolution into the binder. That is why the carbide particles possess an angular morphology, a linear interface with the matrix, and a crystal structure pertinent to WC as identified by SAD pattern.

Figure 9 compares WC size distribution and mean free path of the matrix for different coatings. The latter is measured using the following equation (Ref 36):

$$L = \frac{(1-f)}{N_1}, \tag{Eq 4}$$

where L is the mean free path of the matrix, N_1 is the number of carbides intersected by a line of unit length, and f is the fraction of dispersed carbides determined from the cross-section BSE image. The average of 20 measurements is reported as mean free path for each coating. It is observed that WC size in mc-WC coating varies in a wide range of below ~3 μm with a majority of 600-800 nm (Fig. 9a) indicating a smaller size compared to the initial mc-WC powders (1-6 μm). This results from WC fragmentation due to the high speed impact to the substrate during HVOF process. The mean free path of cobalt matrix for mc-WC coating is measured to be 280 nm. As for nc-WC coating (Fig. 9b), most of the carbide particles have the size of 300-400 nm representing remarkably larger grains with respect to the initial nc-WC (5-30 nm) powder. The extensive grain growth which occurred in nc-WC coating arises mainly from the high temperature of HVOF flame resulting in the coalescence of adjacent nanostructured WC to form larger carbide particles (Ref 12, 18). Compared to mc-WC, lower mean free path of 165 nm was found for nc-WC coating because of the smaller carbide particles (Ref 8). In the case of Ni/nc-WC coating, a large proportion of carbides possess the particle size of ~50-100 nm which is much smaller than that of nc-WC coating (Fig. 9c). This finding is also supported by TEM observation of Ni/nc-WC coating (Fig. 8f). Therefore, it is evident that extensive nanostructured WC grain growth during HVOF process is suppressed by using Ni/nc-WC feedstock powders. As mentioned earlier, on account of the protective role of nickel layer, nanostructured

WC experiences lower flame temperature causing the grain growth of small grains to be hindered. Due to the smaller carbide particles, the lowest mean free path of 70 nm is obtained for Ni/nc-WC among other coatings.

3.2.2 Mechanical and Tribological Properties. The mechanical properties of the coatings in terms of Vickers micro-hardness, indentation fracture toughness, and elastic modulus are presented in Table 6.

The mc-WC coating shows micro-hardness of 1120 Hv, while higher values of 1185 and 1214 Hv were obtained for nc-WC and Ni/nc-WC coatings, respectively. It is well established that the micro-hardness of WC-Co coatings is a balance of several factors including WC grain size and distribution, W_2C content, inter-splat bonding, and the coating porosity (Ref 9, 37). The higher micro-hardness of nc-WC compared to mc-WC coating results from finer WC distribution within the matrix, larger amount of hard W_2C phase, and solid solution strengthening of the Co matrix by W and C due to the extensive dissolution of nc-WC during spraying (Ref 37) . The most scattered micro-hardness data are obtained for nc-WC coating as a consequence of high inhomogeneity of microstructure as depicted in Fig. 8(a, b). Although the Ni/nc-WC coating contains negligible W_2C and W-rich Co binder phase, this coating exhibits slightly higher micro-hardness than nc-WC coating. This is attributed to the lower porosity of Ni/nc-WC (~0.5%) compared to nc-WC coating (Ref 37-39). Besides, the presence of nanostructured and ultrafine WC particles hinders the mobility of dislocations leading to the higher micro-hardness for Ni/nc-WC coating based on Hall-Petch equation (Ref 7, 9).

The Ni/nc-WC coating exhibits the fracture toughness of 10.32 MPa m$^{1/2}$ which is significantly higher than that of mc-WC (5.76 MPa m$^{1/2}$) and nc-WC (5.12 MPa m$^{1/2}$) coatings. It is obvious that the fracture toughness decreases by increasing the extent of WC decarburization, in agreement with the data reported elsewhere (Ref 10, 18, 39). The higher decarburization level results in the larger amounts of brittle W_2C and η phases as well as tungsten-rich cobalt regions, which reduce the fracture toughness of WC-Co coatings; therefore, the Ni/nc-WC coating with minor decarburization exhibits an enhanced
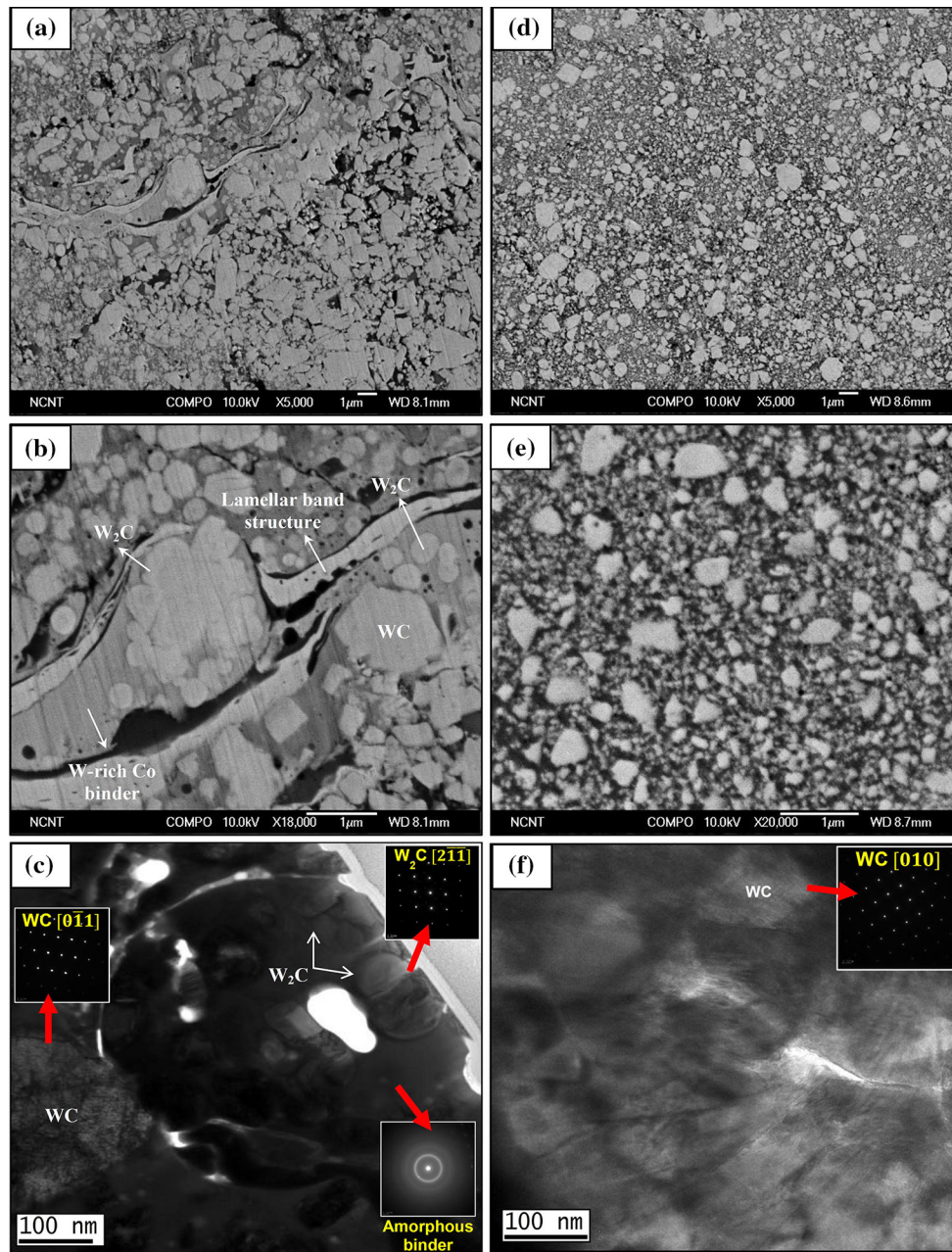
Fig. 8 BSE images from microstructure of nc-WC coating at different magnifications (a, b). Bright-field TEM image and SAD patterns of nc-WC coating (c); BSE images from microstructure of Ni/nc-WC coating at different magnifications (d, e). Bright-filed TEM image and SAD pattern of Ni/nc-WC coating (f)

resistance to crack propagation during indentation. Moreover, homogeneous distribution of nanostructured and ultrafine WC particles in the Ni/nc-WC coating and its lower mean free path (Fig. 9c) provide a greater constraint against deformation of the metallic matrix (Ref 8); consequently, higher amounts of energy are required for crack propagation during indentation resulting in the higher fracture toughness for Ni/nc-WC coating (Ref 40).

The average elastic modulus of Ni/nc-WC coating was measured to be 345 GPa, which is higher than that of mc-WC (310 GPa) and nc-WC (300 GPa). This finding is

in good agreement with the results obtained by Bartuli et al. (Ref 40) and Chivavibul et al. (Ref 8) indicating that the presence of smaller WC particles causes higher elastic modulus for WC-Co coatings.

Figure 10 compares the sliding wear rate and friction coefficient profile for different coatings tested under a constant load of 30 N.

As shown in Fig. 10(a), the Ni/nc-WC coating exhibits a minimum wear rate of 2.5×10^{-4} mg/m whereas higher wear rates of 10.1×10^{-4} and 14.7×10^{-4} mg/m were obtained for mc-WC and nc-WC coatings, respectively. It
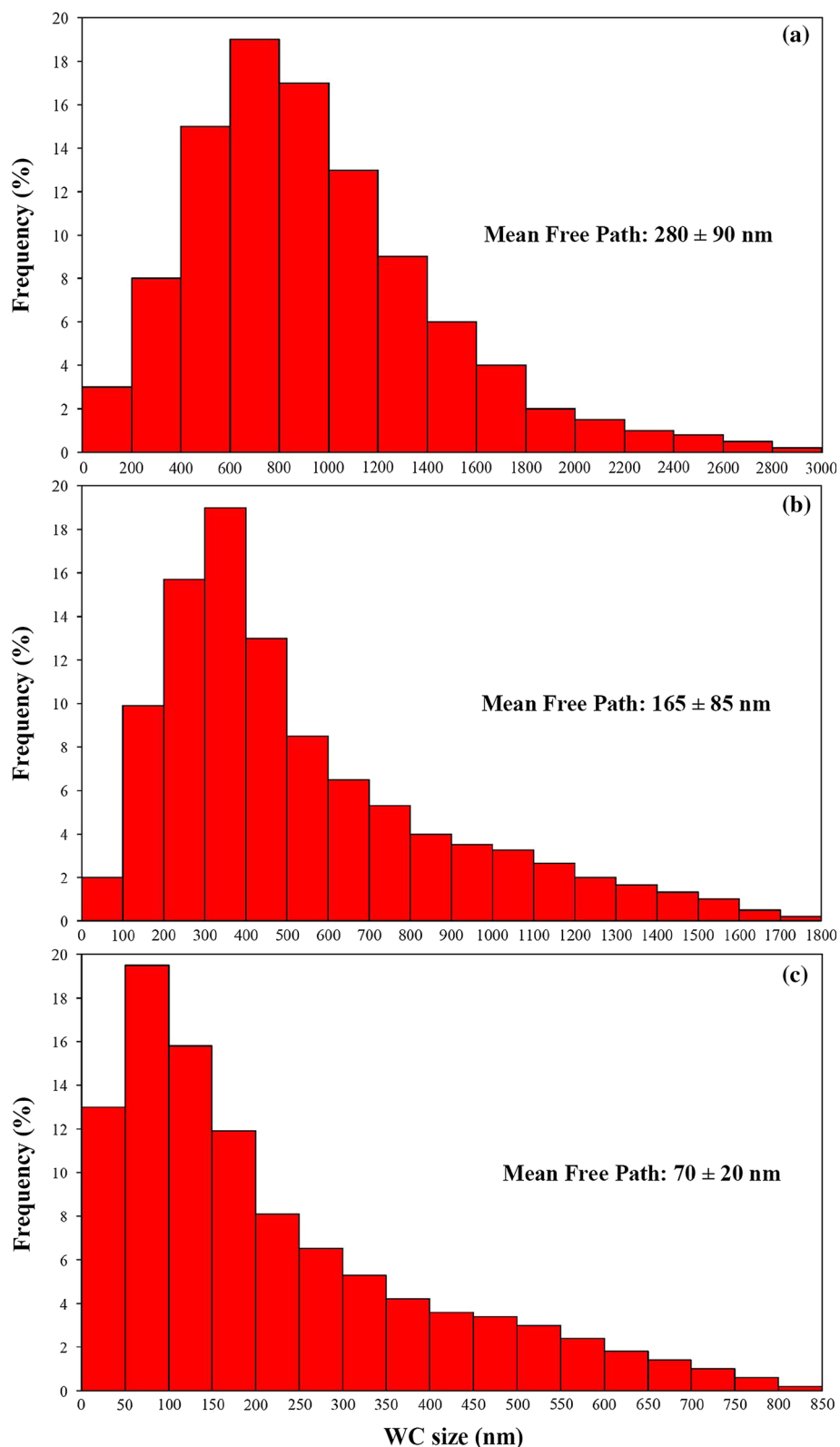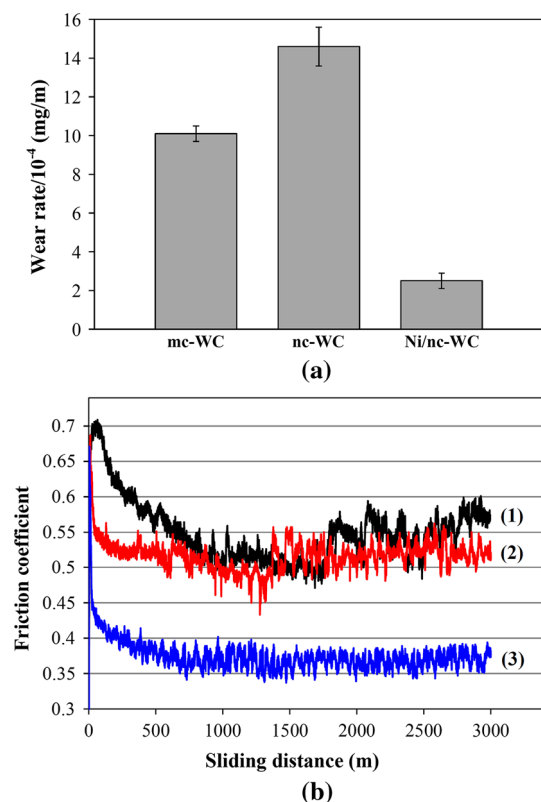
Fig. 9 The WC size distribution and mean free path of the matrix for (a) mc-WC, (b) nc-WC, and (c) Ni/nc-WC coatings

is observed that the wear rate is decreased by about 75 and 82% utilizing Ni/nc-WC coating with respect to mc-WC and nc-WC coatings. The friction coefficient of mc-WC coating shows a relatively long-term running in period of ~1000 m, after which reaches a steady-state range of 0.5-0.6 with a slight tendency for growth. In the case of nc-WC

Table 6 Mechanical properties of the coatings

Coating	Micro-hardness (Hv)	K_{IC} (MPa m$^{1/2}$)	Elastic modulus (GPa)
mc-WC	1120 ± 54	5.76 ± 1.24	300 ± 10
nc-WC	1185 ± 72	5.12 ± 1.3	310 ± 16
Ni/nc-WC	1214 ± 25	10.32 ± 0.4	345 ± 8

Fig. 10 (a) Sliding wear rates and (b) variation of friction coefficient for mc-WC, nc-WC, and Ni/nc-WC coatings

through delamination, pitting, and severe carbide pullout can be observed on the worn surface, which results in more significant materials loss from wear track and higher wear rate in comparison to mc-WC coating (see Fig. 10a). The BSE image and EDS analysis (Fig. 11e, f) also confirm the formation of a tribo-reaction layer containing a mixture of materials from abraded coating and alumina counterface.

In the sliding wear test, materials transfer from alumina counterface to the coatings surface occurs by adhesive wear. This is verified by formation of tribo-reaction layer containing considerable amounts of Al element, as evidenced by EDS analysis (Fig. 11c, f). As the test continues, the repeated compressive and tensile loadings applied on the coating surface by the rotation of alumina ball results in the crack initiation at the sub-surface where the maximum shear stress exists (Ref 41, 42). The cracks propagate along the brittle W_2C and W-rich Co binder phases, which are considered as preferential paths for crack propagation (Ref 8, 14, 43), and form a network of sub-surface cracking. This is followed by large-scale materials removal from the wear track of mc-WC and nc-WC coatings through delamination mechanism. The tribo-reaction layers are also subjected to cracking and delamination as shown in BSE images of mc-WC and nc-WC coatings (Fig. 11b, e). Considering this phenomenon, it is suggested that continuous formation and delamination of tribo-reaction layers during sliding test change the applied load on the coatings surface consequently leading to the high oscillations in the profile of friction coefficient for both mc-WC and nc-WC coatings as illustrated in Fig. 10(b). A severe carbide pullout mechanism also contributes to the wear of nc-WC coating as depicted in Fig. 11(d). This is due to the larger extent of brittle W-rich Co regions in nc-WC coating microstructure, which tend to crack and to be removed during sliding. Hence, the support of the matrix is no longer present for WC particles in some areas donating to the high wear rate of nc-WC coating.

The mc-WC, nc-WC, and Ni/nc-WC coating undergoes a limited carbide pullout following the elimination of Ni (Co) matrix during sliding test, while the evidences of cracking and delamination are not visible on the worn surface of this coating (Fig. 12a).

This originates from negligible decarburization during spraying combined with uniform distribution of fine WC particles with the Ni (Co) matrix, both of which improve the resistance to crack propagation. Moreover, the BSE image from worn surface of Ni/nc-WC (Fig. 12b) reveals no significant evidences of tribo-reaction layer on the wear track. It is proposed that the ultrafine and nanostructured carbide particles supported by Ni (Co) matrix act as the load-bearing components during sliding test causing the matrix removal to be postponed. Thus, the presence of fine WC particles inside the Ni (Co) matrix with strong bonding not only decreases the sliding wear rate to a large extent (Fig. 10a) but also reduces the actual area of surface contact between the coating and alumina ball leading to the low friction coefficient with minor fluctuations (Ref 44). This is verified by EDS analysis which represents

coating, a marginally lower friction coefficient range of 0.5-0.55 is obtained. In contrast, the Ni/nc-WC coating presents the lowest friction coefficient of ~0.35-0.4 with minor fluctuations as compared to that of mc-WC and nc-WC coatings. Therefore, one can conclude that the Ni/nc-WC coating outperforms mc-WC and nc-WC coatings in terms of sliding friction and wear behavior.

To clearly evaluate the wear behavior of the coatings, the worn surfaces were examined by SEM-EDS. As illustrated in Fig. 11(a), the mc-WC coating suffers from sub-surface cracking and subsequent delamination and pit formation. The BSE image (Fig. 11b) shows the presence of tribo-reaction layer with dark contrast on the wear track of mc-WC coating. The EDS analysis (Fig. 11c) proves that the tribo-reaction layer consists mainly of tungsten, cobalt, aluminum, carbon, and oxygen, implying that this layer is formed by mixing the materials removed from the coating and asperities of alumina ball during sliding test. As for nc-WC (Fig. 11d), an extensive damage
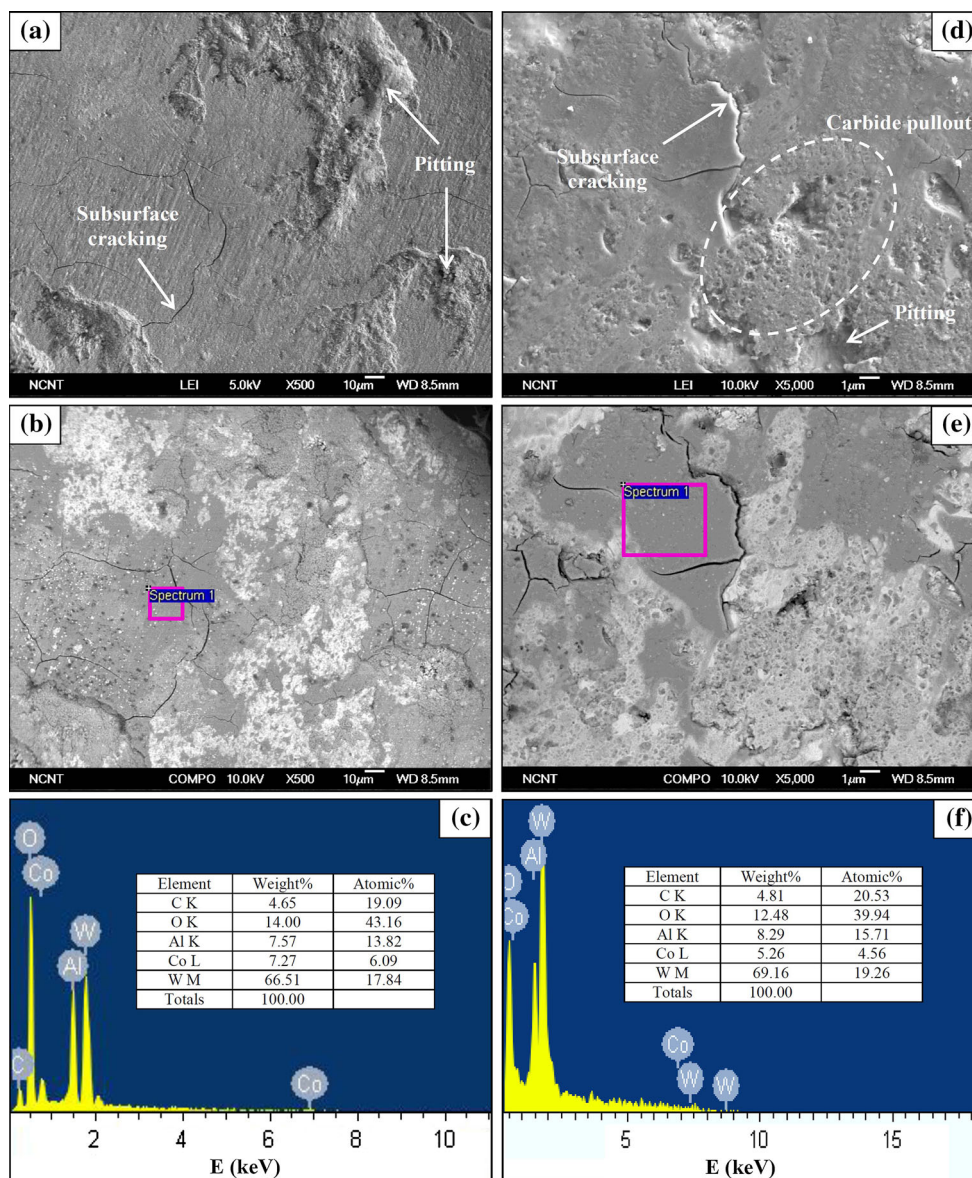
Fig. 11 The SEM and BSE images, and EDS analyses from worn surface of (a-c) mc-WC, (d-f) nc-WC coatings

a very small amount of Al element (~2 at.%) on the worn surface, indicating negligible materials transfer from alumina ball to wear track of Ni/nc-WC coating. At longer times, some carbide particles are pulled out from the regions where the metallic matrix is eliminated. The pullout mechanism is more pronounced for larger carbide particles because they provide more effective moments during rotation of alumina counterface (Ref 40). Therefore, it is concluded that individual carbide pullout is the predominant mechanism of wear for Ni/nc-WC coating.

4. Conclusions

The aim of this research was to investigate the effect of a novel nickel-coated nanostructured WC-12Co feedstock powder (Ni/nc-WC) on microstructural, mechanical, and tribological properties of HVOF-sprayed WC-Co coatings. The results showed that the Ni/nc-WC powder undergoes a negligible decarburization of 5.4% during HVOF owing to the protection role of nickel layer around individual particles, indicating 66 and 85% decrease in the extent of decarburization as compared to mc-WC and nc-WC, respectively. Furthermore, the protective nickel layer suppressed the extensive nanostructured WC grain growth in the case of Ni/nc-WC coating by reducing the interaction between the carbides and HVOF flame; hence, a large proportion of carbides in the case of Ni/nc-WC coating had particle size of ~50-100 nm, much smaller than those for nc-WC coating (300-400 nm). The Ni/nc-WC coating showed improved mechanical properties in terms of micro-hardness, fracture toughness, and elastic modulus
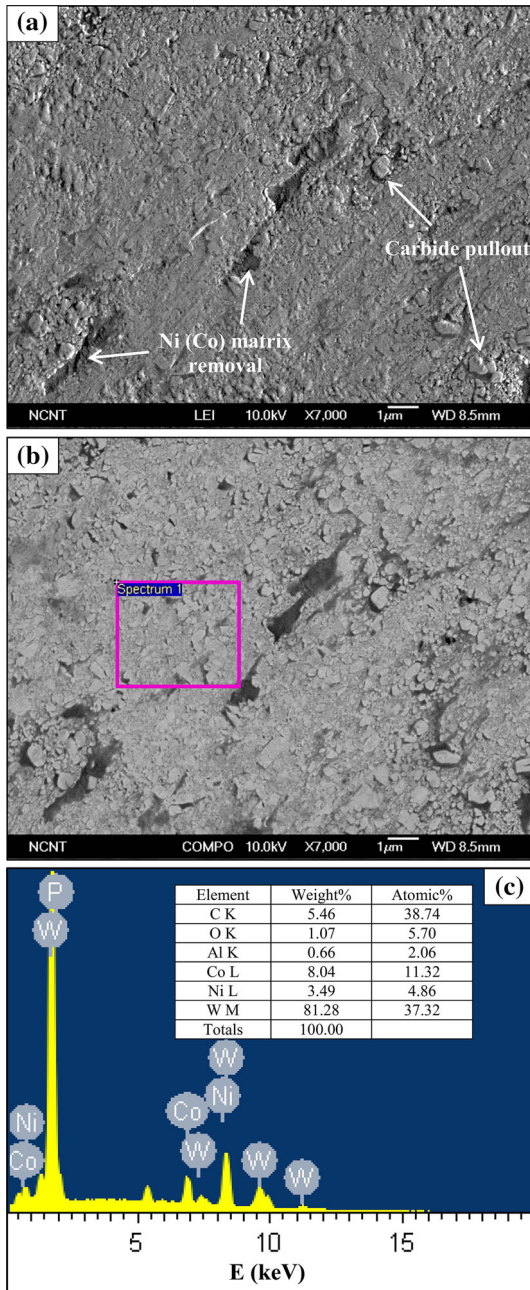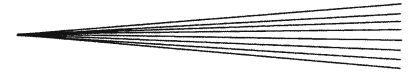
Peer Reviewed

Element	Weight%	Atomic%
C K	5.46	38.74
O K	1.07	5.70
Al K	0.66	2.06
Co L	8.04	11.32
Ni L	3.49	4.86
W M	81.28	37.32
Totals	100.00	

Fig. 12 The SEM (a) and BSE images (b) and EDS analysis (c) from worn surface of Ni/nc-WC coating

with respect to mc-WC and nc-WC coatings. Comparing the sliding wear behavior of the coatings revealed the lowest wear rate and friction coefficient for Ni/nc-WC coating. The SEM-EDS examination of the worn surface showed a large-scale materials removal from the wear track of mc-WC and nc-WC coatings through delamination mechanism. Also, a severe carbide pullout mechanism contributed to the wear of nc-WC coating. In contrast, individual carbide pullout following the elimination of Ni (Co) matrix was the predominant wear mechanism for Ni/nc-WC coating.

References

1. S.A. Hewitt, T. Laoui, and K.A. Kibble, Effect of milling Temperature on the Synthesis and Consolidation of Nanocomposite WC-10Co Powders, *Int. J. Refract. Met. Hard Mater.*, 2009, **27**, p 66-73
2. A.S. Kurlov, A.A. Rempel, Y.V. Blagoveshenskii, A.V. Samokhin, and Y.V. Tsvetkov, Hard Alloys WC-Co (6 wt.%) and WC-Co (10 wt.%) Based on Nanocrystalline Powders, *Dokl. Chem.*, 2011, **439**, p 213-218
3. D.S. Janisch, W. Lengauer, K. Rödiger, K. Dreyer, and H. Van den Berg, Cobalt Capping: Why is Sintered Hardmetal Sometimes Covered with Binder?, *Int. J. Refract. Met. Hard Mater.*, 2010, **28**, p 466-471
4. C. Pang, Z. Guo, J. Luo, T. Hou, and J. Bing, Effect of Vanadium on Synthesis of WC Nanopowders by Thermal Processing of V-Doped Tungsten Precursor, *Int. J. Refract. Met. Hard Mater.*, 2010, **28**, p 394-398
5. C.J. Li and G.J. Yang, Relationships Between Feedstock Structure, Particle Parameter, Coating Deposition, Microstructure and Properties for Thermally Sprayed Conventional and Nanostructured WC-Co, *Int. J. Refract. Met. Hard Mater.*, 2013, **39**, p 2-17
6. A. Mateen, G.C. Saha, T.I. Khan, and F.A. Khalid, Tribological Behaviour of HVOF Sprayed Near-Nanostructured and Microstructured WC-17 wt.%Co Coatings, *Surf. Coat. Technol.*, 2011, **206**, p 1077-1084
7. G.C. Saha and T.I. Khan, The Corrosion and Wear Performance of Microcrystalline WC-10Co-4Cr and Near-Nanocrystalline WC-17Co High Velocity Oxy-Fuel Sprayed Coatings on Steel Substrate, *Metal. Mater. Trans. A*, 2010, **41A**, p 3000-3009
8. P. Chivavibul, M. Watanabe, S. Kuroda, and K. Shinoda, Effects of Carbide Size and Co Content on the Microstructure and Mechanical Properties of HVOF-Sprayed WC-Co Coatings, *Surf. Coat. Technol.*, 2007, **202**, p 509-521
9. J.M. Guilemany, S. Dosta, and J.R. Miguel, The Enhancement of the Properties of WC-Co HVOF Coatings Through the Use of Nanostructured and Microstructured Feedstock Powders, *Surf. Coat. Technol.*, 2006, **201**, p 1180-1190
10. Y. Qiao, T.E. Fischer, and A. Dent, The Effects of Fuel Chemistry and Feedstock Powder Structure on the Mechanical and Tribological Properties of HVOF Thermal-Sprayed WC-Co Coatings with Very Fine Structures, *Surf. Coat. Technol.*, 2003, **172**, p 24-41
11. G. Skandan, R. Yao, R. Sadangi, B.H. Kear, Y. Qiao, L. Liu, and T.E. Fischer, Multimodal Coatings: A New Concept in Thermal Spraying, *J. Therm. Spray. Technol.*, 2000, **9**(3), p 329-331
12. A.K. Basak, J.P. Celis, M. Vardavoulias, and P. Matteazzi, Effect of Nanostructuring and Al Alloying on Friction and Wear Behaviour of Thermal Sprayed WC-Co Coatings, *Surf. Coat. Technol.*, 2012, **206**, p 3508-3516
13. K.H. Baik, J.H. Kim, and B.G. Seong, Improvements in Hardness and Wear Resistance of Thermally Sprayed WC-Co Nanocomposite Coatings, *Mater. Sci. Eng. A*, 2007, **449--451**, p 846-849
14. D.A. Stewart, P.H. Shipway, and D.G. McCartney, Abrasive Wear Behaviour of Conventional and Nanocomposite HVOF-Sprayed WC-Co Coatings, *Wear*, 1999, **225**, p 789-798
15. D.A. Stewart, P.H. Shipway, and D.G. McCartney, Microstructural Evolution in Thermally Sprayed WC-Co Coatings: Comparison Between Nanocomposite and Conventional Starting Powders, *Acta Mater.*, 2000, **48**, p 1593-1604
16. A.H. Dent, S. DePalo, and S. Sampath, Examination of the Wear Properties of HVOF Sprayed Nanostructured and Conventional WC-Co Cermets with Different Binder Phase Contents, *J. Therm. Spray Technol.*, 2002, **11**(4), p 551-558
17. W. Żórawski, The Microstructure and Tribological Properties of Liquid-Fuel HVOF Sprayed Nanostructured WC-12Co Coatings, *Surf. Coat. Technol.*, 2013, **220**, p 276-281
18. H. Wang, X. Song, X. Liu, C. Wei, Y. Gao, and J. Fu, Effect of Heat-Treatment of Spray-Dried Powder on Properties of Ultrafine-Structured WC-Co Coating, *Surf. Coat. Technol.*, 2012, **207**, p 117-122
19. S.L. Liu, X.P. Zheng, and G.Q. Geng, Influence of Nano-WC-12Co Powder Addition in WC-10Co-4Cr AC-HVAF Sprayed

Coatings on Wear and Erosion Behaviour, *Wear*, 2010, **269**, p 362-367

20. N.S. Lim, S. Das, S.Y. Park, M.C. Kim, and C.G. Park, Fabrication and Microstructural Characterization of Nano-Structured WC/Co Coatings, *Surf. Coat. Technol.*, 2010, **205**, p 430-435

21. Z.G. Ban and L.L. Shaw, Characterization of Thermal Sprayed Nanostructured WC-Co Coatings Derived from Nanocrystalline WC-18 wt.%Co Powders, *J. Therm. Spray Technol.*, 2003, **2**(1), p 112-119

22. W. Tillmann, E. Vogli, I. Baumann, G. Matthaeus, and T. Ostrowski, Influence of the HVOF Gas Composition on the Thermal Spraying of WC-Submicron Powders $(-8+1 \mu m)$ to Produce Superfine Structured Cermet Coatings, *J. Therm. Spray Technol.*, 2008, **17**, p 924-932

23. www.schloetter.de/en/processes/18-electroless-nickel

24. A.R. Stokes and A.J.C. Wilson, A Method of Calculating the Integral Breadths of Debye-Scherrer Lines, *Proc. Camb. Philos. Soc.*, 1942, **38**, p 313-322

25. H.H. Tian and M. Atzmon, Comparison of X-Ray Analysis Methods Used to Determine the Grain Size and Strain in Nanocrystalline Materials, *Phil. Mag. A*, 1999, **79**(8), p 1769-1786

26. K. Niihara, A Fracture Mechanics Analysis of Indentation-Induced Palmqvist Crack in Ceramics, *J. Mater. Sci. Lett.*, 1983, **2**, p 221-223

27. W.C. Oliver and G.M. Pharr, An Improved Technique for Determining Hardness and Elastic Modulus Using Load and Displacement Sensing Indentation Experiments, *J. Mater. Res.*, 1992, **7**, p 1564-1583

28. S.A. Hewitt and K.A. Kibble, Effects of Ball Milling Time on the Synthesis and Consolidation of Nanostructured WC-Co Composites, *Int. J. Refract. Met. Hard Mater.*, 2009, **27**, p 937-948

29. J. He, M. Ice, S. Dallek, and E.J. Lavernia, Synthesis of Nanostructured WC-12 Pct Co Coating Using Mechanical Milling and High Velocity Oxygen Fuel Thermal Spraying, *Metall. Mater. Trans. A*, 2000, **31A**, p 541-553

30. M.S. El-Eskandarany, A.A. Mahday, H.A. Ahmed, and A.M. Amer, Synthesis and Characterizations of Ball-Milled Nanocrystalline WC and Nanocomposite WC-Co Powders and Subsequent Consolidations, *J. Alloys Compd.*, 2000, **312**, p 315-325

31. M. Palaniappa and M. Roy, Surface engineering for enhanced performance against wear, *Plating and Tribology*, M. Roy, Ed., Springer, Wien, 2013, p 193-227

32. T.S.N. Sankara Narayanan, I. Baskaran, K. Krishnaveni, and S. Parthiban, Deposition of Electroless Ni-P Graded Coatings and Evaluation of their Corrosion Resistance, *Surf. Coat. Technol.*, 2006, **200**, p 3438-3445

33. Y.D. He, H.F. Fu, X.G. Li, and W. Gao, Microstructure and Properties of Mechanical Attrition Enhanced Electroless Ni-P Plating on Magnesium Alloy, *Scripta Mater.*, 2008, **58**, p 504-507

34. J.M. Guilemany, J.M. de Paco, J. Nutting, and J.R. Miguel, Characterization of the W_2C Phase Formed During the High Velocity Oxygen Fuel Spraying of a WC+12 Pct Co Powder, *Metall. Mater. Trans. A*, 1999, **30A**, p 1913-1921

35. D.A. Stewart, P.H. Shipway, and D.G. McCartney, Influence of Heat Treatment on the Abrasive Wear Behaviour of HVOF Sprayed WC-Co Coatings, *Surf. Coat. Technol.*, 1998, **105**, p 13-24

36. S. Usmani, S. Sampath, D.L. Houck, and D. Lee, Effect of Carbide Grain Size on the Sliding and Abrasive Wear Behavior of Thermally Sprayed WC-Co Coatings, *Tribol. Trans.*, 1997, **40**, p 470-478

37. J.M. Guilemany, S. Dosta, J. Nin, and J.R. Miguel, Study of the Properties of WC-Co Nanostructured Coatings Sprayed by High-Velocity Oxyfuel, *J. Therm. Spray Technol.*, 2005, **11**(4), p 405-413

38. S. Bouaricha and B. Marple, Phase Structure—Mechanical Property Relationship in HVOF-Sprayed WC-12Co Coatings. *Proceedings of the International Thermal Spray Conference* 3-87155-792-7, Osaka Japan (2004)

39. H. Chen, G. Gou, M. Tu, and Y. Liu, Characteristics of Nano Particles and their Effect on the Formation of Nanostructures in Air Plasma Spraying WC-17Co Coating, *Surf. Coat. Technol.*, 2009, **203**, p 1785-1789

40. C. Bartuli, T. Valente, F. Cipri, E. Bemporad, and M. Tului, Parametric study of an HVOF Process for the Deposition of Nanostructured WC-Co Coatings, *J. Therm. Spray Technol.*, 2005, **14**(2), p 187-195

41. J. Yuan, Y. Zhu, X. Zheng, Q. Ruan, and H. Ji, Improvement in Tribological Properties of Atmospheric Plasma-Sprayed WC-Co Coating Followed by Cu Electrochemical Impregnation, *Appl. Surf. Sci.*, 2009, **255**, p 7959-7965

42. J. Yuan, Y. Zhu, X. Zheng, H. Ji, and T. Yang, Fabrication and Evaluation of Atmospheric Plasma Spraying WC-Co-Cu-MoS_2 Composite Coatings, *J. Alloys Compd.*, 2011, **509**, p 2576-2581

43. Y.C. Zhu, K. Yukimura, C.X. Ding, and P.Y. Zhang, Tribological Properties of Nanostructured and Conventional WC-Co Coatings Deposited by Plasma Spraying, *Thin Solid Films*, 2001, **388**, p 277-282

44. Q. Yang, T. Senda, and A. Ohmori, Effect of Carbide Grain Size on Microstructure and Sliding Wear Behavior of HVOF-Sprayed WC-12%Co Coatings, *Wear*, 2003, **254**, p 23-34